

SUBMILLIMETER STUDIES OF PRESTELLAR CORES AND PROTOSTARS: PROBING THE INITIAL CONDITIONS FOR PROTOSTELLAR COLLAPSE

Philippe André¹, Jeroen Bouwman¹, Arnaud Belloche^{1,2}, and Patrick Hennebelle^{2,3}

¹CEA Saclay, Service d'Astrophysique, Orme des Merisiers, Bât. 709, F-91191 Gif-sur-Yvette Cedex, France

²Laboratoire de Radioastronomie, ENS, 24 rue Lhomond, F-75231 Paris Cedex 05, France

³Department of Physics & Astronomy, Cardiff University, Cardiff CF24 3YB, Wales, UK

ABSTRACT

Improving our understanding of the initial conditions and earliest stages of protostellar collapse is crucial to gain insight into the origin of stellar masses, multiple systems, and protoplanetary disks. Observationally, there are two complementary approaches to this problem: (1) studying the structure and kinematics of prestellar cores observed prior to protostar formation, and (2) studying the structure of young (e.g. Class 0) accreting protostars observed soon after point mass formation. We discuss recent advances made in this area thanks to (sub)millimeter mapping observations with large single-dish telescopes and interferometers. In particular, we argue that the beginning of protostellar collapse is much more violent in cluster-forming clouds than in regions of distributed star formation. Major breakthroughs are expected in this field from future large submillimeter instruments such as Herschel and ALMA.

Key words: ISM: structure – ISM: gravitational collapse – Stars: protostellar accretion rates

1. INTRODUCTION

Although the formation of low-mass stars is now reasonably well understood in outline (see, e.g., Mannings, Boss, & Russell 2000 for recent reviews), several important aspects remain poorly known, such as the initial stages of the collapse process, the mechanism(s) selecting stellar masses, or the formation of multiple systems. Some progress on the earliest stages of star formation was achieved over the last decade thanks to the use of sensitive receivers on large (sub)millimeter radiotelescopes such as JCMT, CSO, and the IRAM 30m. Young protostars were identified at the beginning of the main accretion phase (Class 0 objects – André, Ward-Thompson, & Barsony 1993), and the starless dense cores extensively studied in NH₃ by Myers and collaborators (e.g. Benson & Myers

1989) were found to be characterized by flat inner density gradients (Ward-Thompson et al. 1994). Direct evidence for infall motions was observed toward a large number of Class 0 protostars and prestellar cores (e.g. Gregersen et al. 1997 – see § 3 below and Evans, this volume). Class 0 objects were also found to drive more powerful outflows than more evolved (Class I) protostars, suggesting a marked decrease of the mass accretion/ejection rates in the course of protostellar evolution (Bontemps et al. 1996). As advocated by Henriksen, André, & Bontemps (1997), there may be a causal relationship between these results, in the sense that the accretion/ejection decline during the protostellar phase may be a direct consequence of the form of the density profile at the prestellar stage. Further studying the detailed properties of prestellar cores and young protostars is of prime importance to distinguish between collapse models and shed light on the origin of stellar masses. Indeed, the effective reservoirs of mass available for the formation of individual stars may be largely determined at the prestellar stage, and it is during the main protostellar accretion phase that stars accrete some fraction of these reservoirs and build up the masses they will have on the zero-age main sequence.

After a brief introduction of the theoretical background (§ 1.1), we review recent observational advances concerning the density and velocity structure of cloud cores in § 2 and § 3, respectively. We conclude in § 4 with a comparison between observations and theoretical models.

1.1. COLLAPSE INITIAL CONDITIONS: THEORY

The inside-out collapse model of Shu (1977), starting from a singular isothermal sphere (SIS) or toroid (cf. Li & Shu 1996, 1997), is well known and underlies the ‘standard’ picture of isolated, low-mass star formation (e.g. Shu, Adams, & Lizano 1987).

Other collapse models exist, however, which adopt different initial conditions. In particular, Whitworth & Summers (1985) have shown that there is a two-parameter continuum of similarity solutions to the problem of isother-

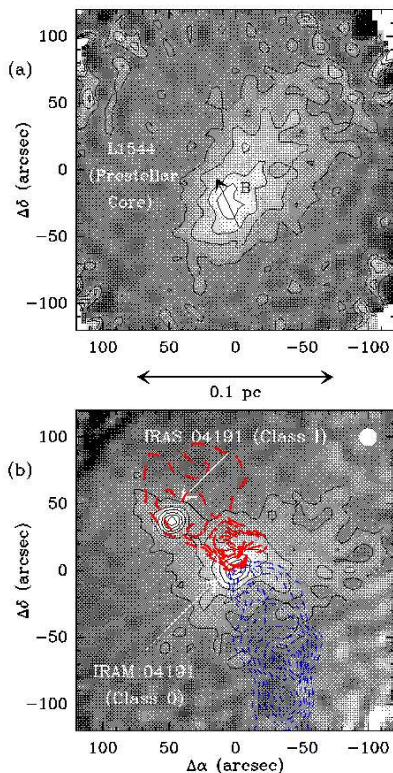


Figure 1. Dust continuum maps of L1544 (a) and IRAM 04191 (b) at 1.3 mm taken with the IRAM 30 m telescope and the MPIfR bolometer array (from Ward-Thompson et al. 1999 and André et al. 1999, respectively). Effective resolution: $13''$; base contour and contour step: 20 mJy/beam. The direction of the magnetic field measured in L1544 with the SCUBA polarimeter on JCMT (Ward-Thompson et al. 2000) and the collimated CO(2-1) bipolar flow emanating from IRAM 04191 are shown.

mal spherical collapse. One of the parameters measures how close to hydrostatic equilibrium the system is initially, while the other parameter reflects how important external compression is in initiating the collapse. In this continuum, the solutions proposed by Shu (1977) and Larson (1969)-Penston (1969) represent two extreme limits. All of the similarity solutions share a universal evolutionary pattern. At early times ($t < 0$), a compression wave (initiated by, e.g., an external disturbance) propagates inward leaving behind it a $\rho(r) \propto r^{-2}$ density profile. At $t = 0$, the compression wave reaches the cen-

ter and a point mass forms which subsequently grows by accretion. At later times ($t > 0$), this wave is reflected into a rarefaction or expansion wave, propagating outward through the infalling gas (at the isothermal sound speed a_s), and leaving behind it a free-fall $\rho(r) \propto r^{-1.5}$ density distribution. Several well-known features of the Shu model (such as the expansion wave) are thus in fact common to all solutions. The various solutions can be distinguished by the *absolute* values of the density and velocity at $t \sim 0$. In particular, the Shu (1977) solution has $\rho(r) = (a_s^2/2\pi G) r^{-2}$ and is static ($v = 0$) at $t = 0$, while the Larson-Penston (1969) solution is ~ 4.4 times denser and far from equilibrium ($v \approx -3.3 a_s$). During the accretion phase ($t > 0$), the infall envelope is a factor ~ 7 denser in the Larson-Penston solution. Accordingly, the mass infall rate is also much larger in the Larson-Penston case ($\sim 47 a_s^3/G$) than in the Shu case ($\sim a_s^3/G$).

In practice, however, protostellar collapse is unlikely to be strictly self-similar, and the above similarity solutions can only be taken as plausible asymptotes. More realistic initial conditions than the SIS are provided by the so-called ‘Bonnor-Ebert’ spheres (e.g. Bonnor 1956), which represent the equilibrium states for self-gravitating isothermal spheres and have a flat density profile in their central \sim Jeans length region. Such spheres are stable for a center-to-edge density contrast < 14.3 and unstable for a density contrast > 14.3 (e.g. Bonnor 1956). Numerical hydrodynamic simulations of cloud collapse starting from such initial conditions (e.g. Foster & Chevalier 1993, Hennebelle et al. 2002) find that the Larson-Penston similarity solution is generally a good approximation near point-mass formation ($t = 0$) at *small radii*, but that the Shu solution is more adequate at intermediate $t \geq 0$ times, before the expansion wave reaches the edge of the initial, pre-collapse dense core. In general, the mass accretion rate is thus expected to be time-dependent.

Observationally, it is by comparing the (density and velocity) structure of prestellar cores such as L1544 (see Fig. 1a) with the structure of the envelopes surrounding Class 0 protostars such as IRAM 04191 (cf. Fig. 1b) that one may hope to constrain the initial conditions for collapse and to discriminate between the various existing models.

2. DENSITY STRUCTURE

2.1. PRESTELLAR CORES

Two main approaches have been used to trace the density structure of cloud cores: (1) mapping the optically thin (sub)millimeter continuum *emission* from the cold dust

contained in the cores, and (2) mapping the same cold core dust in *absorption* against the background infrared emission (originating from warm cloud dust or remote stars). Mapping the molecular gas component is generally less effective as most molecules tend to freeze out onto dust grains in the dense, cold inner parts of cloud cores (e.g. Kramer et al. 1999, Walmsley et al. 2001, Bacmann et al. 2002, and Bergin 2002).

Ward-Thompson et al. (1994, 1999) and André et al. (1996) employed the first approach to probe the structure of prestellar cores (see also Shirley et al. 2000). Under the simplifying assumption of spatially uniform dust (temperature and emissivity) properties, they concluded that the radial density profiles of isolated prestellar cores were *not* consistent with the single $\rho(r) \propto r^{-2}$ power law of the SIS but were flatter than $\rho(r) \propto r^{-1}$ in their inner regions (for $r \leq R_{flat}$), and approached $\rho(r) \propto r^{-2}$ only beyond a typical radius $R_{flat} \sim 2500\text{--}5000$ AU. The details of this conclusion have been challenged by Evans et al. (2001) and Zucconi et al. (2001) who made the important point that starless cores are not strictly isothermal. Accounting for a realistic temperature distribution inside the cores (see § 2.3 below), these authors found smaller values for R_{flat} and even claimed that in some cases the observed profiles could not be distinguished from a SIS profile. We will return to this point below (e.g. § 2.3).

More recently, it has been possible to use the *absorption* approach, both in the mid-IR from space (e.g. Bacmann et al. 2000, Siebenmorgen & Krügel 2000) and in the near-IR from the ground (e.g. Alves et al. 2001). In particular, using the ISOCAM infrared camera aboard the *ISO* satellite, Bacmann et al. (2000) carried out a $7\ \mu\text{m}$ survey of 24 low-mass starless cores (all undetected by *IRAS*) and observed absorption features in 23 of them. As an example, Fig. 2a shows the ISOCAM image obtained at $6.75\ \mu\text{m}$ for the prestellar core L1689B in the Ophiuchus complex ($d \sim 150$ pc). The core is seen in absorption against the diffuse mid-IR background arising from the rear side of the parent molecular cloud (e.g. Bernard et al. 1993, see also § 2.3 below).

The column density structure of the absorbing cores can be derived from a simple modeling of the ISOCAM observations. The mid-IR intensity measured at projected radius \bar{r} from core center may be expressed as:

$$I(\bar{r}) = I_{back} \cdot e^{-\tau(\bar{r})} + I_{fore}, \quad (1)$$

where τ is the core optical depth (directly related to the column density N_{H_2} via the dust opacity) and I_{back} and I_{fore} are the background and foreground intensities, respectively. Both I_{back} and I_{fore} are uncertain but their values are well constrained when independent millimeter

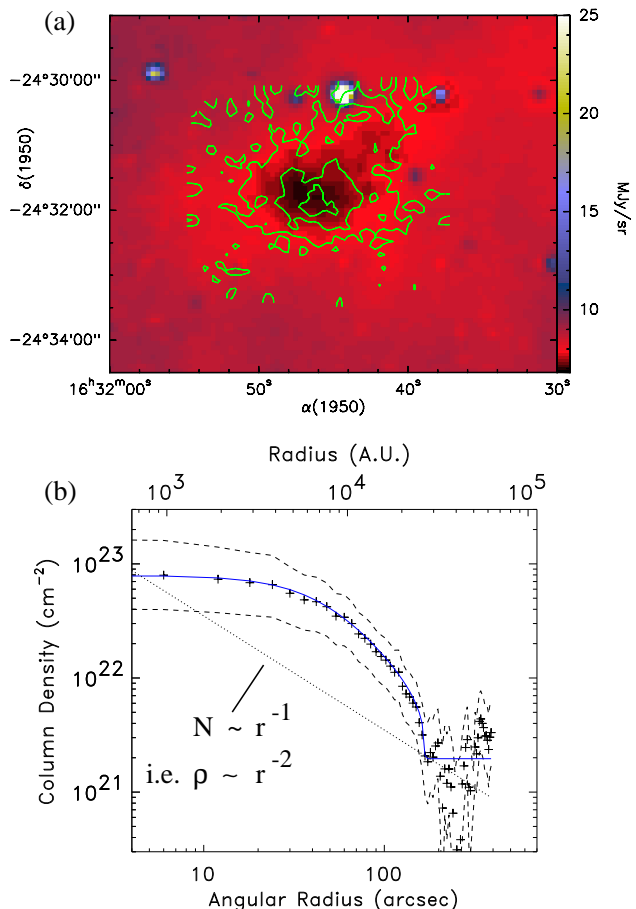


Figure 2. (a) ISOCAM $6.75\ \mu\text{m}$ absorption image of the prestellar core L1689B (see color scale on the right in MJy/sr). The $1.3\ \text{mm}$ continuum emission map obtained by André et al. (1996) at the IRAM 30 m telescope is superposed as green contours (levels: 10, 30, 50 $\text{mJy}/13''$ beam). (b) Column density profile of L1689B (crosses) derived from the absorption map shown in (a) by averaging the intensity over elliptical annuli for a 40° sector in the southern part of the core. The dashed curves show the most extreme profiles compatible with the data given the uncertainties affecting the absorption analysis. The blue, solid curve represents the best fit of a Bonnor-Ebert sphere model (embedded in a medium of uniform column density), obtained with the following parameters: $\rho_c/\rho_{out} = 40 \pm 15$ (i.e., well into the unstable regime), $T_{eff} = 50 \pm 20\ \text{K}$, $P_{ext}/k_B = 5 \pm 3 \times 10^5\ \text{K cm}^{-3}$. For comparison, the dotted line shows the $N_{H_2} \propto \bar{r}^{-1}$ profile of a SIS at $T = 10\ \text{K}$. (Adapted from Bacmann et al. 2000.)

measurements of the H_2 column density in the centers and outer parts of the cores are available (see Bacmann et al. 2000 for details).

Using these constraints on I_{back} and I_{fore} , a range of possible column density profiles can be derived for each core imaged in absorption with ISOCAM. This is shown in Fig. 2b for L1689B, where the crosses display our ‘best’ estimate of the column density profile (derived using a revised estimate of $8 \times 10^{22} \text{ cm}^{-2}$ for the central column density from millimeter continuum data, in agreement with a central temperature of $\sim 8 \text{ K}$ – see § 2.3 below – instead of 12.5 K as assumed by Bacmann et al. 2000). The dashed curves lying above and below the ‘best’ profile show the most extreme column density profiles that are consistent with the mid-IR absorption data, given the range of permitted values for I_{back} and I_{fore} . In general, four different regimes can be distinguished on the prestellar column density profiles (see, e.g., Fig. 2b):

a) a flat inner region (of radius $R_{flat} = 5000 \pm 1000 \text{ AU}$ for L1689B according to the fitting analysis shown in Fig. 2b), b) a region roughly consistent with $N_{\text{H}_2} \propto \bar{r}^{-1}$ (corresponding to $\rho \propto r^{-2}$ for a spheroidal core), c) an edge where the column density falls off typically more rapidly than $N_{\text{H}_2} \propto \bar{r}^{-2}$ with projected radius (suggesting a density gradient steeper than $\rho \propto r^{-3}$), until d) the end of the core is reached (at $R_{out} = 28000 \pm 1000 \text{ AU}$ for L1689B) and N_{H_2} fluctuates about the mean value $N_{out} \sim 1 - 2 \times 10^{21} \text{ cm}^{-2}$ characterizing the ambient molecular cloud.

A qualitatively similar column density profile was derived by Alves et al. (2001) for the Bok globule B68 (for which $R_{flat} \approx 4000 \text{ AU}$ and $R_{out} \approx 12500 \text{ AU}$), based on VLT and NTT measurements of the near-IR colors of background stars seen through, and suffering extinction from, this globule.

Thus, the *inner flattening of the density profiles of prestellar cores* first observed in submillimeter emission (see above) is confirmed by infrared absorption/extinction measurements, which are essentially *independent of the temperature distribution*. Moreover, a new result emerges: at least in some cases, such as L1689B and B68, isolated prestellar cores appear to be characterized by *sharp edges* defining typical outer radii $R_{out} \sim 20000 \text{ AU} \sim 0.1 \text{ pc}$.

2.2. COMPARISON WITH THEORETICAL MODELS

These observed features, i.e., flat inner region and sharp outer edge, set constraints on possible models of core structure. First of all, it is clear that self-similar, singular models such as the SIS or magnetized, non-spherical

generalizations of it (e.g. Shu 1977, Li & Shu 1996), cannot account for the detailed density structure of prestellar cores. As pointed out by Bacmann et al. (2000), the logotropic models of McLaughlin & Pudritz (1996), which behave as $\rho \propto r^{-1}$ over a wide range of radii, are also inconsistent with the observations of (low-mass) starless cores. On the other hand, the circularly-averaged column density profiles can often be fitted remarkably well with models of pressure-bounded Bonnor-Ebert spheres, as first demonstrated by Alves et al. (2001) for B68. This is also the case of L1689B as illustrated in Fig. 2b. The quality of such fits shows that Bonnor-Ebert spheres provide a good, first order model for the structure of isolated prestellar cores. In detail, however, there are several problems with these Bonnor-Ebert models. First, most starless cores exhibit elongated shapes (see, e.g., Fig. 1a and Fig. 2a) which are not consistent with spherical models beyond $\sim 0.03 \text{ pc}$. Second, the inferred density contrasts (from center to edge) are generally larger (i.e., $\gtrsim 20-80$ – see Fig. 2b) than the maximum contrast of ~ 14 for a stable Bonnor-Ebert sphere (cf. § 1.1). Third, the effective core temperature needed in these models (for thermal pressure gradients to balance self-gravity) is often significantly larger than both the average dust temperatures measured with ISOPHOT (e.g. Ward-Thompson et al. 2002) and the gas temperatures measured in NH_3 (e.g. Lai et al., this volume). In the case of L1689B, for instance, the effective temperature of the Bonnor-Ebert fit shown in Fig. 2b is $T_{eff} \sim 50 \text{ K}$, while the dust temperature observed with ISOPHOT is only $T_d \sim 11 \text{ K}$ (Ward-Thompson et al. 2002). Finally, the physical process responsible for bounding the cores at some external pressure is unclear. These arguments suggest that prestellar cores cannot be described as simple isothermal hydrostatic structures and are either already contracting (see § 3.1 below) or experiencing extra support from static or turbulent magnetic fields (e.g. Curry & McKee 2000).

One way of accounting for large density contrasts and high effective temperatures is to consider models of cores threaded by a static magnetic field and evolving through ambipolar diffusion (e.g. Ciolek & Mouschovias 1994, Basu & Mouschovias 1995). In these models, at any given time prior to protostar formation, the cores are expected to feature a uniform-density central region whose size corresponds to the instantaneous Jeans length. This agrees well with the characteristics of the flat inner regions seen in starless cores. Furthermore, the observed sharp edges (e.g. Fig. 2b) are consistent with the model predictions (shortly) after the formation of a magnetically supercritical core. Physically, this is because when a supercriti-

cal core forms, it collapses dynamically inward, while the outer, subcritical envelope is still efficiently supported by the magnetic field and remains essentially “held in place”. As a result, a steep density profile develops at the outer boundary of the supercritical core (see Fig. 8 of Basu & Mouschovias 1995).

A problem, however, with these ambipolar diffusion models involving only a static magnetic field is that they require fairly large field strengths ($\sim 30\text{--}100\ \mu\text{G}$, see Bacmann et al. 2000), which seem to exceed the (few) existing Zeeman measurements for low-mass dense cores (e.g. Crutcher 1999, Crutcher & Troland 2000). It is possible that more elaborate versions of the models, incorporating the effects of a non-static, turbulent magnetic field in the outer parts of the cores and in the ambient cloud, would be more satisfactory and could also account for the filamentary shapes often seen on large ($\gtrsim 0.25\ \text{pc}$) scales (cf. Curry 2000, 2002 and Jones & Basu 2002).

2.3. TEMPERATURE DISTRIBUTION IN STARLESS CORES

The models discussed in § 2.2 above assume that prestellar cores are isothermal, which is quite a good first approximation (e.g. Larson 1969, Tohline 1982). In actual fact, however, there are good reasons to believe that the central regions of starless cores are somewhat cooler than their outer regions. Indeed, the results of *ISO* imaging in the mid-IR (Bacmann et al. 2000) and far-IR (Ward-Thompson et al. 2002) are consistent with the idea that starless cores are heated only from outside by the local interstellar radiation field (ISRF): the amount of energy radiated by such cores in the far-IR is roughly equal to the fraction of ISRF energy absorbed at shorter (e.g. mid-IR) wavelengths, with no evidence for any central heating source (Ward-Thompson et al. 2002). In such a situation, recent dust radiative transfer calculations (Evans et al. 2001; Zucconi et al. 2001) predict that there should be a positive temperature gradient from the cores’ centers (with T_d as low as $\sim 5\text{--}7\ \text{K}$) to their edges (at $T_d \sim 15\ \text{K}$). [Note that, in the dense ($n_{\text{H}_2} > 3 \times 10^4\ \text{cm}^{-3}$) inner regions, one expects the temperature of the gas to be well coupled to that of the dust (e.g. Doty & Neufeld 1997).] The first calculations published by Evans et al. (2001) and Zucconi et al. (2001) assumed rather a simplistic input radiation field, based on current estimates of the average radiation field in the solar neighborhood (e.g. Black 1994). We have more recently carried out similar calculations in which we use the levels of the diffuse mid-IR and far-IR backgrounds observed toward the cores to make more realistic estimates of the effective radiation field di-

rectly impinging on their surfaces. Fig. 3a gives an illustration for the prestellar core L1689B already discussed in § 2.1 (see Fig. 2). In this case, the radiation field differs (in strength and spectrum) from the Black standard radiation field for several reasons: (1) due to the presence of early-type stars such as HD 147889 (B2 V) only a few parsecs away from the Ophiuchus cloud (e.g. Liseau et al. 1999), the ambient far-UV field is significantly stronger (i.e., $G_0 \sim 12$) than the solar neighborhood average; (2) this strong FUV field in turn excites small PAH-like grains in the outer ($A_V \lesssim 1$) layers of the cloud which are responsible for a high level of diffuse mid-IR emission distributed in several spectral bands (cf. Bernard et al. 1993 and Fig. 3a); (3) the L1689B core is itself embedded at some depth ($A_V \sim 1$) inside the cloud, so that a good fraction of the external FUV radiation is effectively reprocessed to longer wavelengths. Consequently, the effective radiation field for L1689B is about *one order of magnitude stronger* in both the mid-IR and the far-IR than the Black radiation field (cf. Fig. 3a), in agreement with the strong mid-IR and far-IR backgrounds measured by Bacmann et al. (2000) and Ward-Thompson et al. (2002) with ISOCAM and ISOPHOT ($\sim 4\ \text{MJy/sr}$ at $7\ \mu\text{m}$ and $\sim 120\ \text{MJy/sr}$ at $200\ \mu\text{m}$, as opposed to $\sim 0.25\ \text{MJy/sr}$ and $\sim 30\ \text{MJy/sr}$, respectively, in the Black radiation field). Based on this estimate of the effective radiation field, we have used the MODUST radiative transfer code (e.g. Bouwman 2001, Kemper et al. 2001) to compute the temperature distribution in the L1689B core for several plausible density distributions consistent with the 1.3 mm continuum emission map of André et al. (1996) and the $7\ \mu\text{m}$ absorption map of Bacmann et al. (2000). The results are illustrated in Fig. 3b.

Our calculations confirm some of the conclusions of Evans et al. (2001) and Zucconi et al. (2001), namely that the temperature reaches a minimum $< 10\ \text{K}$ in the centers of prestellar cores and that the central temperature depends primarily on the central optical depth (directly related to the degree of shielding from the external ISRF). However, we find that the minimum temperature may not be as low as reported by Evans et al. (2001) and Zucconi et al. (2001) and that the shape of the temperature profile may be quite different: it can be seen in Fig. 3b that the major drop in temperature occurs in the outer parts of the core in our preferred model of L1689B (red curve), while it occurs closer to the center in the Evans et al. (2001) model (dashed curve). We also stress that all of the models we have run have a relatively high mass-averaged dust temperature of $\sim 11\ \text{K}$, comparable to the temperature estimated by fitting a grey-

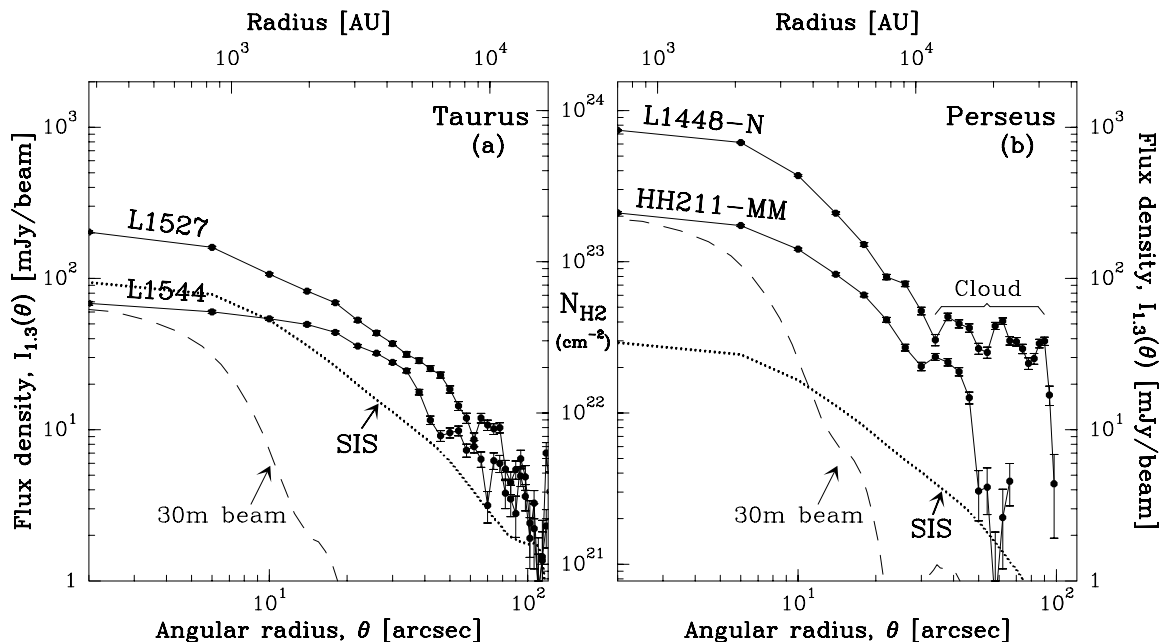


Figure 5. Averaged 1.3 mm radial intensity profiles of (a) L1544 (prestellar) and L1527 (Class 0) in Taurus ($d = 140$ pc), and (b) HH211-MM and L1448-N (Class 0s) in Perseus ($d = 350$ pc), compared to a synthetic profile, simulated for a singular isothermal sphere (SIS) model at $T = 10$ K (see Appendix of Motte & André 2001 for details about such simulations). The profile of the 30m beam is shown. An approximate column density scale, calculated assuming representative dust properties ($T_d = 15$ K, $\kappa_{1.3} = 0.0075$ cm² g⁻¹) is also indicated. (Adapted from Ward-Thompson et al. 1999 and Motte & André 2001.)

body to the global SED (cf. Fig. 13 of Ward-Thompson et al. 2002). (Note that Doty & Palotti 2002 have independently reached a similar conclusion.) Furthermore, if our assumptions about the effective radiation field and the dust opacity law (see Fig. 3b) are correct, then the radius of the flat inner region in the density profile of L1689B must lie between $R_{flat} = 3300$ AU (smallest value consistent with the 1.3 mm constraints of André et al. 1996) and $R_{flat} = 6600$ AU (value found by Bacmann et al. 2000 assuming a central core temperature of 12.5 K – see § 2.1). A value as small as $R_{flat} = 2000$ AU (cf. Evans et al. 2001) is ruled out according to our analysis. Thus, conclusions derived from (sub)millimeter emission maps on the density structure of prestellar cores under the simplifying hypothesis that the dust temperature is uniform (e.g. Ward-Thompson et al. 1999) are probably not seriously flawed.

In our opinion, the final word on the structure of prestellar cores will come from high-resolution mapping at far-IR and submillimeter wavelengths with future spaceborne telescopes such as *Herschel* to be launched by ESA in 2007 (e.g. Pilbratt et al. 2001). Using *Herschel* images at 75–500 μ m (in combination with ground-based

dust continuum mapping at longer submillimeter wavelengths) to construct SED maps for at least the nearest, spatially resolved prestellar cores, it will be possible to reconstruct their *intrinsic temperature and density distributions simultaneously* as illustrated in Fig. 4. Such multi-band mapping observations will also set strong constraints on the *dust emissivity properties* (e.g. the opacity index β) and their spatial variation across dense cores.

2.4. STRUCTURE OF PROTOSTELLAR ENVELOPES

In the case of *protostellar* envelopes, the accretion luminosity released close to the central protostar provides an additional source of heating compared to starless cores. In practice, however, the thermal structure of the envelopes surrounding low-luminosity protostars ($L_{bol} \lesssim 1\text{--}10 L_{\odot}$), including most Taurus embedded YSOs, is strongly affected by external heating from the ambient ISRF (Shirley et al. 2002), and the simple isothermal assumption (with $T \simeq 10$ K) is often not too bad over a wide range of radii ($r \sim 3000\text{--}15000$ AU – cf. Motte & André 2001).

The density structure of YSO envelopes has been studied primarily with the (sub)millimeter emission approach

(although see Harvey et al. 2001 for a recent extinction study). In contrast to prestellar cores, protostellar envelopes are always found to be strongly centrally condensed (see, e.g., Fig. 1b) and do *not* exhibit any marked inner flattening in their radial (column) density profiles. This is illustrated in Fig. 5 which shows the circularly-averaged radial intensity profiles measured at 1.3 mm for the circumstellar envelopes of the Class 0 objects L1527 in Taurus and HH211-MM and L1448-N in Perseus (Motte & Andr 2001). (Note that the inner disk contribution has been subtracted from the profiles based on high-resolution interferometric measurements with the IRAM Plateau de Bure interferometer.) Apart from a small overdensity factor (~ 2), the profile of the L1527 envelope closely follows the *shape* of the SIS model profile (see Fig. 5a), and is significantly steeper than the profile of the prestellar core L1544 at small radii.

More generally, several (sub)millimeter continuum studies indicate that protostellar envelopes in regions of isolated star formation such as Taurus have radial density gradients consistent with $\rho(r) \propto r^{-p}$ with $p \sim 1.5-2$ over more than $\sim 10000-15000$ AU in radius (e.g. Ladd et al. 1991, Chandler & Richer 2000, Hogerheijde & Sandell 2000, Shirley et al. 2000, Motte & Andr 2001, Jørgensen et al. 2002). The density gradient estimated for (Class 0 and Class I) protostars (i.e., $p \sim 1.5-2$) agrees with most collapse models which predict a value of p between 2 and 1.5 during the protostellar accretion phase (before and after the passage of the collapse expansion wave, respectively – see § 1.1 above). Furthermore, the median envelope mass measured by Motte & André (2001) for the bona-fide protostars of Taurus [$\overline{M_{env}}(r < 4200 AU) \sim 0.3 M_{\odot}$] is roughly consistent with the predictions of the inside-out collapse model of Shu (1977) for $\sim 10^5$ yr-old protostars.

The situation is markedly different in regions where stars form in tight groups or *clusters*, such as Serpens, Perseus, and the ρ Oph main cloud. In this case, the observed envelopes are clearly *not scale-free*: they merge with dense cores, other envelopes, and/or the diffuse ambient cloud at a *finite* radius $R_{out} \lesssim 5000$ AU (Motte, André, & Neri 1998; Motte & André 2001; see also Fig. 5 of Mundy, Looney, & Welch 2000). Moreover, as can be seen in Fig. 5b for HH211-MM and L1448-N, the Class 0 envelopes mapped in cluster-forming regions are found to be *3 to 12 times denser* than the SIS at $T = 10$ K (which is the typical gas kinetic temperature expected in these clouds prior to massive star formation – see Goldsmith & Langer 1978, Evans 1999, Goldsmith 2001, and Fig. 3b). Static magnetic fields can only account for mod-

erate overdensity factors ($\lesssim 2$) compared to an unmagnetized SIS (see Li & Shu 1997). Turbulence could in principle contribute to the support of the initial dense core (e.g. Myers & Fuller 1992, Mardones et al. 1997). However, the small-scale condensations corresponding to the precursors of protostars in star-forming clusters (e.g. Motte et al. 1998) appear to be largely devoid of turbulence (see § 3.1 below). A more likely explanation is that, in such regions, protostellar collapse is *induced by strong external disturbances* and starts from *non-singular initial conditions*, resulting in a *non-equilibrium density configuration* with a large overdensity factor ($\lesssim 10$) and significant inward velocities near $t \sim 0$ (see also § 4 and Fig. 9 below).

3. VELOCITY STRUCTURE

3.1. INTERNAL MOTIONS IN STARLESS CORES

On large (\gtrsim pc) scales, the spectral line profiles/widths observed in molecular clouds are indicative of supersonic turbulent motions (e.g. Falgarone & Phillips 1990). The nonthermal component of the line width, σ_{NT} , roughly follows the scaling law $\sigma_{NT} \propto R^{0.5}$ (e.g. Fuller & Myers 1992), which is believed to arise from MHD turbulence (e.g. Mouschovias & Psaltis 1995). On intermediate ($\gtrsim 0.1$ pc) scales, there are strong differences between the “low-mass” cores observed in regions of distributed star formation (e.g. Taurus), whose line widths are dominated by thermal motions (e.g. Benson & Myers 1989), and the “massive”, cluster-forming cores of, e.g., Ophiuchus and Orion, whose line widths are still dominated by turbulent motions (e.g. Caselli & Myers 1995). On small ($\lesssim 0.03$ pc) scales, however, the prestellar condensations of the Ophiuchus, Serpens, Perseus, and Orion cluster-forming regions are always characterized by very *narrow line widths* (e.g. Belloche et al. 2001, Myers 2001), which is reminiscent of the thermal cores of Taurus. In the ρ Oph protocluster, for instance, the nonthermal velocity dispersion is about half the thermal velocity dispersion of H_2 ($\sigma_{NT}/\sigma_T \sim 0.7$) toward the starless condensations of the dense cores Oph B1, C, E, F (Belloche et al. 2001). This indicates that, *even in cluster-forming clouds*, the initial conditions for individual protostellar collapse are “coherent” (cf. Goodman et al. 1998) and essentially free of turbulence. The dissipation, on small (< 0.1 pc) scales, of a significant fraction of the turbulent motions observed on large scales is thus a prerequisite for the formation of prestellar condensations (e.g. Nakano 1998, Myers 1998, Falgarone & Pety 2001). Apart from low levels of turbulence, low-mass prestellar cores are also characterized by

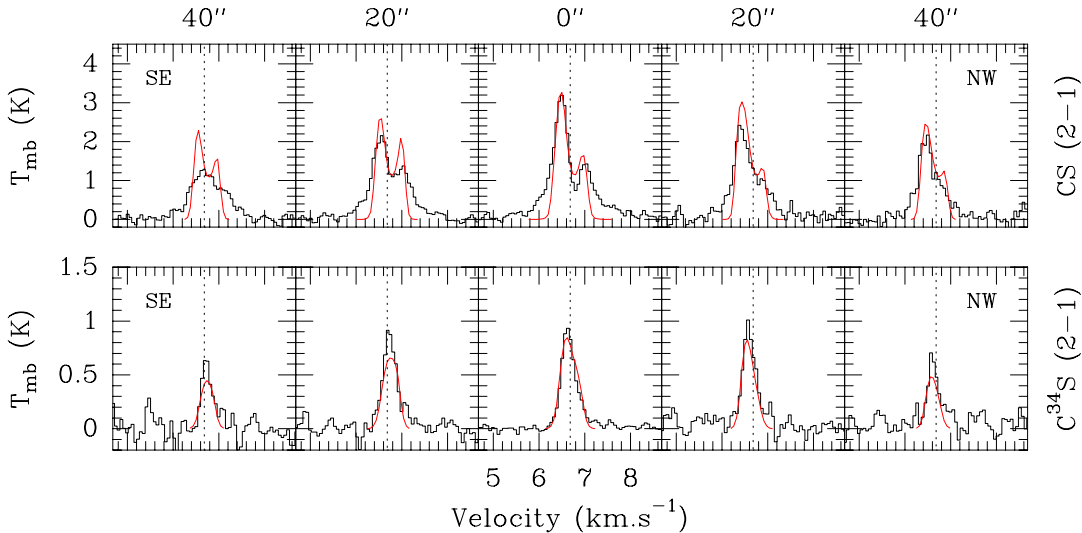


Figure 7. Spectra observed with the IRAM 30m telescope toward IRAM 04191, along the axis perpendicular to the outflow, in the optically thick CS(2–1) and optically thin C³⁴S(2–1) lines. Synthetic spectra corresponding to the ‘best-fit’ collapse model including rotation found by Belloche et al. (2002) are superposed (see text for parameters).

small rotation rates in general ($\Omega \sim 10^{-14} - 10^{-13} \text{ rad s}^{-1}$ – e.g. Goodman et al. 1993), and subsonic, extended infall motions (e.g. Lee, Myers, & Tafalla 2001 – see also Evans, this volume).

3.2. ROTATION AND INFALL IN CLASS 0 OBJECTS

The velocity structure of only a few Class 0 objects has been studied in detail up to now. Here, we mostly discuss the example of the nearby ($d = 140 \text{ pc}$) and relatively isolated Class 0 object IRAM 04191+1522 (IRAM 04191 for short) found by André, Motte, & Bacmann (1999) in the vicinity of the Taurus Class I source IRAS 04191+1523 (e.g. Tamura et al. 1991 – see Fig. 1b).

IRAM 04191 features a very high envelope mass to luminosity ratio ($M_{env}^{<4200 \text{ AU}}/L_{bol} \sim 3 M_{\odot}/L_{\odot}$) and a low bolometric temperature ($T_{bol} \sim 18 \text{ K}$), suggesting an age $t \lesssim 3 \times 10^4 \text{ yr}$ since the beginning of the accretion phase (see André et al. 1999). It is also remarkable in that it has a very low bolometric luminosity ($L_{bol} \sim 0.15 L_{\odot}$), and no or only a tiny accretion disk ($R_{disk} < 15 \text{ AU}$, $M_{disk} < 2 \times 10^{-3} M_{\odot}$). Accordingly, IRAM 04191 is probably the youngest accreting protostar currently known in Taurus.

IRAM 04191 is associated with a flattened circumstellar envelope, seen in the dust continuum (Fig. 1b) and in dense gas tracers such as N₂H⁺, C₃H₂, H¹³CO⁺, and DCO⁺ (Belloche et al. 2002). All of the maps taken in small optical depth lines show a clear velocity gradient across this envelope of $\sim 7 \text{ km s}^{-1} \text{ pc}^{-1}$ increasing from

west to east along the long axis, i.e., roughly perpendicular to the outflow axis (see Fig. 1b and Fig. 6). Strongly suggestive of rotation, this velocity gradient corresponds to a mean angular velocity $\Omega \sim 3 \times 10^{-13} \text{ rad s}^{-1}$ in the inner $\sim 3000 \text{ AU}$ region (after deprojection from a viewing angle $i = 50^\circ$). Furthermore, this rotation does not occur in a rigid-body, but differential, fashion: the inner $\sim 3500 \text{ AU}$ -radius region seems to be rotating significantly faster than the outer parts of the core (see Fig. 6). The ‘S’ shape of the position-velocity diagram shown in Fig. 6 can be fitted with a rotation curve of the form $V_{rot}(r) \propto r^{0.1 \pm 0.4}$ for $r < 3500 \text{ AU}$ and $V_{rot}(r) \propto r^{-1.5 \pm 0.5}$ for $3500 < r < 11000 \text{ AU}$, corresponding to $\Omega(r) \propto r^{-0.9 \pm 0.4}$ and $\Omega(r) \propto r^{-2.5 \pm 0.5}$, respectively (see Fig. 8a and Belloche et al. 2002 for details).

Direct evidence for infall motions over a large portion of the IRAM 04191 envelope is also observed in optically thick lines such as CS(2–1), CS(3–2), H₂CO(2₁₂–1₁₁), and H₂CO(3₁₂–2₁₁). These lines are double-peaked and skewed to the blue up to $\gtrsim 40''$ from source center (see Fig. 7), which is indicative of infall motions up to a radius $R_{inf} \gtrsim 5000 \text{ AU}$ from center (cf. Evans 1999 and Evans, this volume). Radiative transfer modeling confirms this view, suggesting a relatively flat infall velocity profile ($V_{inf} \sim 0.1 \text{ km s}^{-1}$) for $3000 \lesssim r \lesssim 11000 \text{ AU}$ and larger infall velocities scaling as $V_{inf} \propto r^{-0.5}$ for $r \lesssim 3000 \text{ AU}$ (see Fig. 8b and Belloche et al. 2002 for details). The mass infall rate is estimated to be $\dot{M}_{inf} \sim 2 - 3 \times a_s^3/G \sim$

$3 \times 10^{-6} M_{\odot} \text{ yr}^{-1}$ (with $a_s \sim 0.15 - 0.2 \text{ km s}^{-1}$ for $T \sim 6 - 10 \text{ K}$), roughly independent of radius.

Another Class 0 object whose kinematics has been quantified in detail recently is the IRAS 4 system in the NGC 1333 protocluster (Di Francesco et al. 2001). IRAS 4 is a triple system (A/B/C) on scales of $\sim 10000 \text{ AU}$, whose primary component (A) itself breaks up into a $\sim 600 \text{ AU}$ binary (e.g. Looney et al. 2000). Using the IRAM Plateau de Bure interferometer, Di Francesco et al. (2001) observed inverse P-Cygni profiles in $\text{H}_2\text{CO}(3_{12} - 2_{11})$ toward IRAS 4A and IRAS 4B, from which they derived very large mass infall rates of $\sim 1.1 \times 10^{-4} M_{\odot} \text{ yr}^{-1}$ and $\sim 3.7 \times 10^{-5} M_{\odot} \text{ yr}^{-1}$ at $r \sim 2000 \text{ AU}$ for A and B, respectively. Even if a warmer initial gas temperature ($\sim 20 \text{ K}$) than in IRAM 04191 and some initial level of turbulence are accounted for (see Di Francesco et al. 2001), these values of \dot{M}_{inf} correspond to more than ~ 15 and ~ 6 times the canonical a_{eff}^3/G value, respectively (where $a_{\text{eff}} \lesssim 0.3 \text{ km s}^{-1}$ is the effective sound speed). These very high infall rates result both from very dense envelopes (see Motte & André 2001) and large, supersonic infall velocities ($\sim 0.68 \text{ km s}^{-1}$ and $\sim 0.47 \text{ km s}^{-1}$ for A and B, respectively, according to Di Francesco et al. 2001). Evidence of fast rotation, producing a velocity gradient as high as $\sim 40 \text{ km s}^{-1} \text{ pc}^{-1}$, was also found by Di Francesco et al. (2001) toward IRAS 4A.

4. CONCLUSIONS: COMPARISON WITH COLLAPSE MODELS

In the case of low-mass, isolated dense cores, the SIS model of Shu (1977) describes global features of the collapse (e.g. the mass infall rate) reasonably well and thus remains a useful, approximate guide. In detail, however, the extended infall velocity profiles observed in prestellar cores (e.g. Lee et al. 2001) and in the very young Class 0 object IRAM 04191 (§ 3.2 above) are inconsistent with the pure inside-out collapse picture of Shu (1977). The *shape* of the density profiles observed in prestellar cores are well fitted by purely thermal Bonnor-Ebert sphere models, but the *absolute* values of the densities are suggestive of some additional magnetic support (§ 2.2). The observed infall velocities are also marginally consistent with isothermal collapse models starting from Bonnor-Ebert spheres (e.g. Foster & Chevalier 1993, Hennebelle et al. 2002), as such models tend to produce somewhat faster velocities. This suggests that the collapse of ‘isolated’ cores is essentially *spontaneous* and somehow moderated by magnetic effects in magnetized, probably not strictly isothermal Bonnor-Ebert cloudlets. Furthermore, the contrast seen in Fig. 8 between a steeply declining

rotation velocity profile and a flat infall velocity profile beyond $\sim 3500 \text{ AU}$ suggests that angular momentum is *not* conserved in the outer envelope of IRAM 04191. Such a behavior is very difficult to explain in the context of non-magnetic collapse models. In the presence of a relatively strong ($\sim 60 \mu\text{G}$) magnetic field, on the other hand, the outer envelope can be coupled to, and spun down by, the (large moment of inertia of the) ambient cloud (e.g. Basu & Mouschovias 1994). Based on a qualitative comparison with the ambipolar diffusion models of Basu & Mouschovias, Belloche et al. (2002) propose that the rapidly rotating inner envelope of IRAM 04191 corresponds to a magnetically supercritical core decoupling from an environment still supported by magnetic fields and strongly affected by magnetic braking. (Quantitatively, however, the models published so far are rotating too slowly to fit the observations.) In this view, the inner $\sim 3500 \text{ AU}$ radius envelope of IRAM 04191 would correspond to the effective mass reservoir ($\sim 0.5 M_{\odot}$) from which the central star is being built. Moreover, comparison of these results with the rotational characteristics of other objects in Taurus (Ohashi et al. 1997) suggests that IRAM 04191 behaves in a typical manner and is simply observed particularly soon after point mass formation (i.e., at $t \gtrsim 0$). If this is correct, *the masses of the stars forming in clouds such as Taurus may be largely determined by magnetic decoupling effects.*

In protoclusters, by contrast, the large overdensity factors measured for Class 0 envelopes compared to hydrostatic isothermal structures (cf. § 2.4), as well as the fast supersonic infall velocities and very large infall rates observed in some cases (e.g. § 3.2), are inconsistent with self-initiated forms of collapse and require a *strong external influence*. This point is illustrated in Fig. 9 with the results of recent SPH simulations by Hennebelle et al. (2002). These simulations follow the evolution of a Bonnor-Ebert sphere whose collapse has been induced by an increase in external pressure P_{ext} . Large overdensity factors (compared to a SIS), together with supersonic infall velocities, and large infall rates ($\gtrsim 10 a_s^3/G$) are found near $t = 0$ when (and only when) the increase in P_{ext} is strong and very rapid (e.g. Fig. 9b), resulting in a violent compression wave. Such a violent collapse may be conducive to the formation of both massive stars (through higher accretion rates) and multiple systems (when realistic, non-isotropic compressions are considered). Future high-resolution studies with the next generation of (sub)millimeter instruments (e.g., ALMA) will greatly help test this view and shed further light on the physics of collapse in cluster-forming regions.

REFERENCES

- Alves, J.F., Lada, C.J., & Lada, E.A. 2001, *Nature*, 409, 159
- André, P., Motte, F., & Bacmann, A. 1999, *ApJ*, 513, L57
- André, P., Ward-Thompson, D., & Barsony, M. 1993, *ApJ*, 406, 122
- André, P., Ward-Thompson, D., & Motte, F. 1996, *A&A*, 314, 625
- Bacmann, A., André, P., Puget, J.-L., Abergel, A., Bontemps, S., & Ward-Thompson, D. 2000, *A&A*, 361, 555
- Bacmann, A., Lefloch, B., Ceccarelli, C., Castets, A., Steinacker, J., & Loinard, L. 2002, *A&A*, 389, L6
- Basu, S., & Mouschovias, T.C. 1994, *ApJ*, 432, 720
- Basu, S., & Mouschovias, T.C. 1995, *ApJ*, 453, 271
- Benson, P.J., & Myers, P.C. 1989, *ApJSS*, 71, 89
- Belloche, A., Andr, P., & Motte, F. 2001, in *From Darkness to Light*, Eds. T. Montmerle & P. Andr, ASP Conf. Ser., 243, p. 313
- Belloche, A., Andr, P., Despois, D. & Blinder, S. 2002, *A&A*, 393, 927
- Bergin, E.A. 2002, this volume
- Bernard, J.P., Boulanger, F., Puget, J.L. 1993, *A&A*, 277, 609
- Black, J.H. 1994, in *The First Symposium on the Infrared Cirrus and Diffuse Interstellar Clouds*, ASP Conf. Ser., 58, p. 355
- Bonnor, W.B. 1956, *MNRAS*, 116, 351
- Bontemps, S., André, P., Terebey, S., Cabrit, S. 1996, *A&A*, 311, 858
- Bouwman, J. 2001, PhD thesis, University of Amsterdam
- Caselli, P., & Myers, P.C. 1995, *ApJ*, 446, 665
- Chandler, C.J., & Richer, J.S. 2000, *ApJ*, 530, 851
- Ciolek, G.E., & Mouschovias, T.C. 1994, *ApJ*, 425, 142
- Crutcher, R.M. 1999, *ApJ*, 520, 706
- Crutcher, R.M., & Troland, T.H. 2000, *ApJ*, 537, L139
- Curry, C.L. 2000, *ApJ*, 541, 831
- Curry, C.L. 2002, *ApJ*, 576, 849
- Curry, C.L., & McKee, C.F. 2000, *ApJ*, 528, 734
- Di Francesco, J., Myers, P.C., Wilner, D.J., Ohashi, N., & Mardones, D. 2001, *ApJ*, 562, 770
- Doty, S.D., & Neufeld, D.A. 1997, *ApJ*, 489, 122
- Doty, S.D., & Palotti, M.L. 2002, *MNRAS*, 335, 993
- Evans, N.J. II 1999, *ARA&A*, 37, 311
- Evans, N.J. II, Rawlings, J.M.C., Shirley, Y.L., & Mundy, L.G. 2001, *ApJ*, 557, 193
- Falgarone, E., & Pety, J. 2001 in *From Darkness to Light*, Eds. T. Montmerle & P. Andr, ASP Conf. Ser., 243, p. 53
- Falgarone, E., & Phillips, T. 1990, *ApJ*, 359, 344
- Foster, P.N., & Chevalier, R.A. 1993, *ApJ*, 416, 303
- Goldsmith, P.F., Langer, W.D. 1978, *ApJ*, 222, 881
- Goldsmith, P.F. 2001, *ApJ*, 557, 736
- Goodman, A.A., Benson, P.J., Fuller, G.A., & Myers, P.C. 1993, *ApJ*, 406, 528
- Goodman, A.A., Barranco, J.A., Wilner, D.J., Heyer, M.H. 1998, *ApJ*, 504, 223
- Gregersen, E.M., Evans, N.J., Zhou, S., & Choi, M. 1997, *ApJ*, 484, 256
- Harvey, D.W.A., Wilner, D.J., Lada, C.J. et al. 2001, *ApJ*, 563, 903
- Hennebelle, P., Whitworth, A.P., Gladwin, P.P., & Andr, P. 2002, *MNRAS*, in press
- Henriksen, R.N., André, P., & Bontemps, S. 1997, *A&A*, 323, 549
- Hogerheijde, M.R., & Sandell, G. 2000, *ApJ*, 534, 880
- Jones, C.E., & Basu, S. 2002, *ApJ*, 569, 280
- Jørgensen, J.K., Schöier, F.L., & van Dischoeck, E.F. 2002, *A&A*, 389, 908
- Kemper, F., Waters, L.B.F.M., de Koter, A., & Tielens, A.G.G.M. 2001, *A&A*, 369, 132
- Kramer, C., Alves, J., Lada, C.J. et al. 1999, *A&A*, 342, 257
- Ladd, E.F., Adams, F.C., Casey, S. et al. 1991, *ApJ*, 382, 555
- Larson, R.B., 1969, *MNRAS*, 145, 271
- Lee, C.W., Myers, P.C., & Tafalla, M. 2001, *ApJS*, 136, 703
- Li, Z.-Y., & Shu, F.H. 1996, *ApJ*, 472, 211
- Li, Z.-Y., & Shu, F.H. 1997, *ApJ*, 475, 237
- Liseau, R., White, G. J., Larsson, B. et al. 1999, *A&A*, 344, 342
- Looney, L.W., Mundy, L.G., & Welch, W.J. 2000, *ApJ*, 529, 477
- Mardones, D., Myers, P. C., Tafalla, M., Wilner, D. J., Bachiller, R., Garay, G. 1997, *ApJ*, 489, 719
- McLaughlin, D.E., Pudritz, R.E. 1996, *ApJ*, 469, 194
- Motte, F., & Andr, P. 2001, *A&A*, 365, 440
- Motte, F., André, P., & Neri, R. 1998, *A&A*, 336, 150
- Mouschovias, T.Ch., & Psaltis, D. 1995, *ApJ*, 444, L105
- Mundy, L.G., Looney, L.W., & Welch, W.J. 2000, in *Protostars and Planets IV*, Eds. V. Mannings, A.P. Boss, & S.S. Russell (Univ. of Arizona Press, Tucson), p. 355
- Myers, P.C. 1998, *ApJ*, 496, L109
- Myers, P.C. 2001, in *From Darkness to Light*, Eds. T. Montmerle & P. Andr, ASP Conf. Ser., 243, p. 131
- Myers, P.C., & Fuller, G.A. 1992, *ApJ*, 396, 631
- Nakano, T. 1998, *ApJ*, 494, 587
- Ohashi, N., Hayashi, M., Ho, P.T.P., Momose, M., Tamura, M., Hirano, N., & Sargent, A.I. 1997, *ApJ*, 488, 317
- Ossenkopf, V., & Henning, Th. 1994, *A&A*, 291, 943
- Penston, M.V., 1969, *MNRAS*, 144, 425
- Pilbratt, G.L., Cernicharo, J., Heras, A.M., & Prusti, T. (eds.) 2001, *The Promise of FIRST*, ESA SP-460
- Preibisch, Th., Ossenkopf, V., Yorke, H.W., & Henning, Th. 1993, *A&A*, 279, 577
- Shirley, Y., Evans II, N.J., Rawlings, J.M.C., Gregersen, E.M. 2000, *ApJS*, 131, 249
- Shirley, Y., Evans II, N.J., & Rawlings, J.M.C. 2002, *ApJ*, 575, 337
- Shu, F. 1977, *ApJ*, 214, 488
- Shu, F.H., Adams, F.C., & Lizano, S. 1987, *ARA&A* 25, 23
- Siebenmorgen, R., & Krügel, E. 2000, *A&A*, 364, 625
- Tamura, M., Gatley, I., Waller, W., & Werner, M.W. 1991, *ApJ*, 374, L25

- Tohline, J. E. 1982, *Fund. of Cos. Phys.*, 8, 1
- Walmsley, M., Caselli, P., Zucconi, A., & Galli, D. 2001, in *The Origin of Stars and Planets: The VLT View*, Eds. J. Alves & M. McCaughrean (Springer-Verlag, Berlin), *ESO Astrophysics Symposia*, p. 29
- Ward-Thompson, D., André, P., & Kirk, J.M. 2002, *MNRAS*, 329, 257
- Ward-Thompson, D., Kirk, J.M., Crutcher, R.M. et al. 2000, *ApJL*, 537, L135
- Ward-Thompson, D., Motte, F., & André, P. 1999, *MNRAS*, 305, 143
- Ward-Thompson, D., Scott, P.F., Hills, R.E., & André, P. 1994, *MNRAS*, 268, 276
- Whitworth, A., & Summers, D. 1985, *MNRAS*, 214, 1
- Zucconi, A., Walmsley, C.M., & Galli, D., 2001, *A&A*, 376, 650

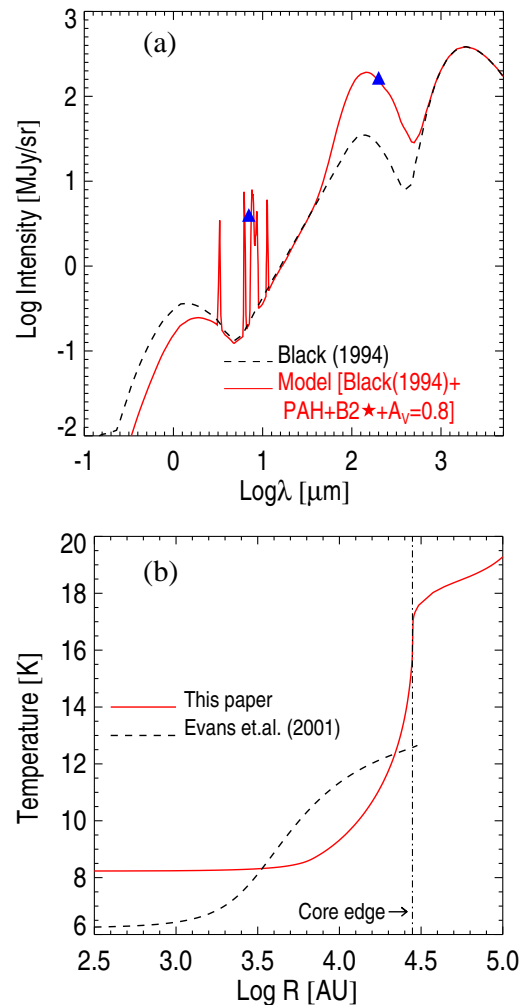


Figure 3. (a) Effective radiation field impinging on L1689B (red, solid curve), as estimated from the observed levels of the mid-IR and far-IR backgrounds (blue triangles, see text). This is much stronger than the Black (1994) radiation field (black, dashed curve). (b) Model dust temperature profiles calculated for L1689B with MODUST under two sets of assumptions: the red, solid curve assumes the effective radiation field shown in (a), the density profile derived by Bacmann et al. (2000) (with $R_{\text{flat}} = 6600$ AU), and the dust opacity law of Preibisch et al. (1993) with thin ice mantles in the core and no ice mantles in the ambient cloud; the black, dashed curve corresponds to the model favored by Evans et al. (2001) which has $R_{\text{flat}} = 2000$ AU (for $d = 160$ pc), no ambient cloud, and assumes the Black (1994) radiation field $\times 0.5$ and the dust opacity law of Ossenkopf & Henning (1994) with coagulation (OH5).

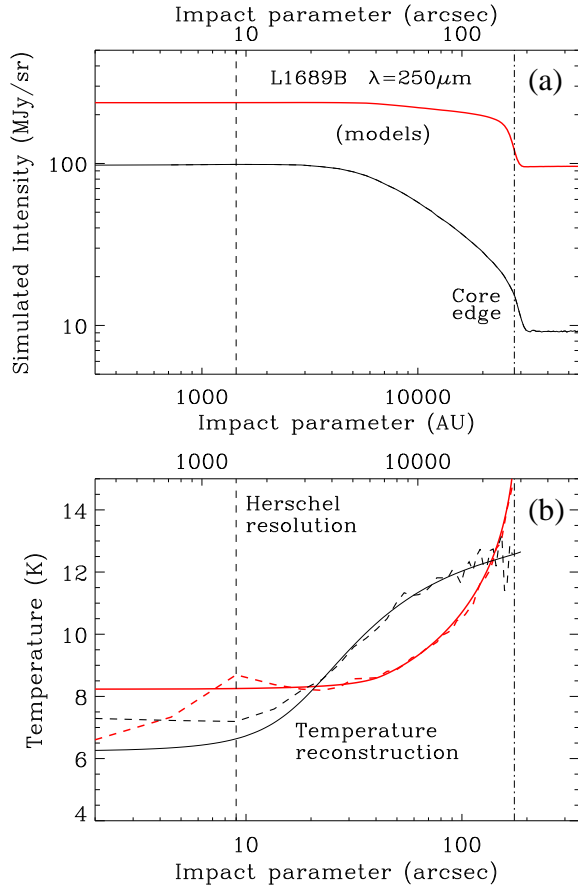


Figure 4. Simulated Herschel observations of the radial structure of the prestellar core L1689B. The top panel (a) shows two model intensity profiles, consistent with present millimeter data, as they could be observed by Herschel at $250\ \mu\text{m}$. The upper (red) curve corresponds to the model we favor here based on our best estimate of the effective radiation field (see Fig. 3), while the lower curve is for the model proposed by Evans et al. (2001) based on the Black (1994) ISRF $\times 0.5$. Note the large differences in shape and absolute scaling between the two models. The bottom panel (b) shows the dust temperature distributions (solid curves) calculated with MODUST for these two models. The dashed curves (almost indistinguishable from the solid curves beyond $20''$) show the reconstructed temperature profiles that could be derived from Herschel maps in 6 bands between $75\ \mu\text{m}$ and $500\ \mu\text{m}$ (plus ground-based data at $850\ \mu\text{m}$ and $1.3\ \text{mm}$), assuming the 3-D core geometry is known. The reconstruction becomes uncertain below the Herschel resolution limit ($9''$ HP beam radius at $250\ \mu\text{m}$).

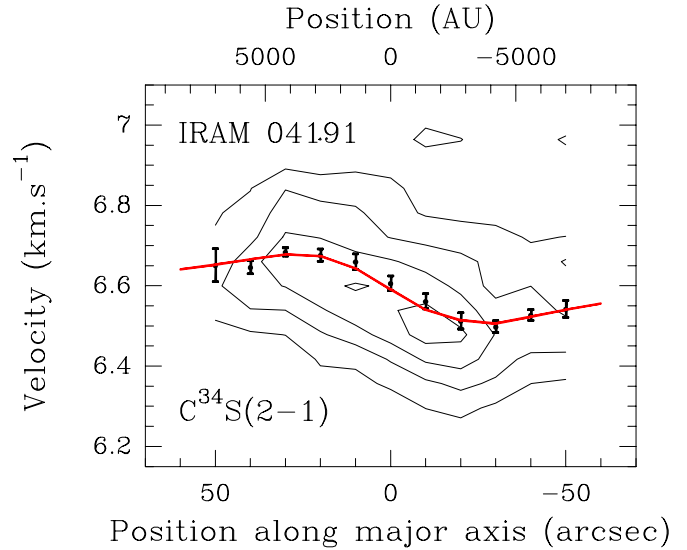


Figure 6. Position-velocity diagram along the major axis of the IRAM 04191 envelope (i.e., perpendicular to the flow) based on a $\text{C}^{34}\text{S}(2-1)$ map taken at the IRAM 30m telescope (Belloche et al. 2002). Contours: 0.2 to 0.8 by 0.2 K. The dots with error bars mark the observed velocity centroids. The solid curve shows the profile of a model with differential rotation ($V_{\text{rot}}(r > 3500\ \text{AU}) \propto r^{-1.5}$) also used in Fig. 7 (see text).

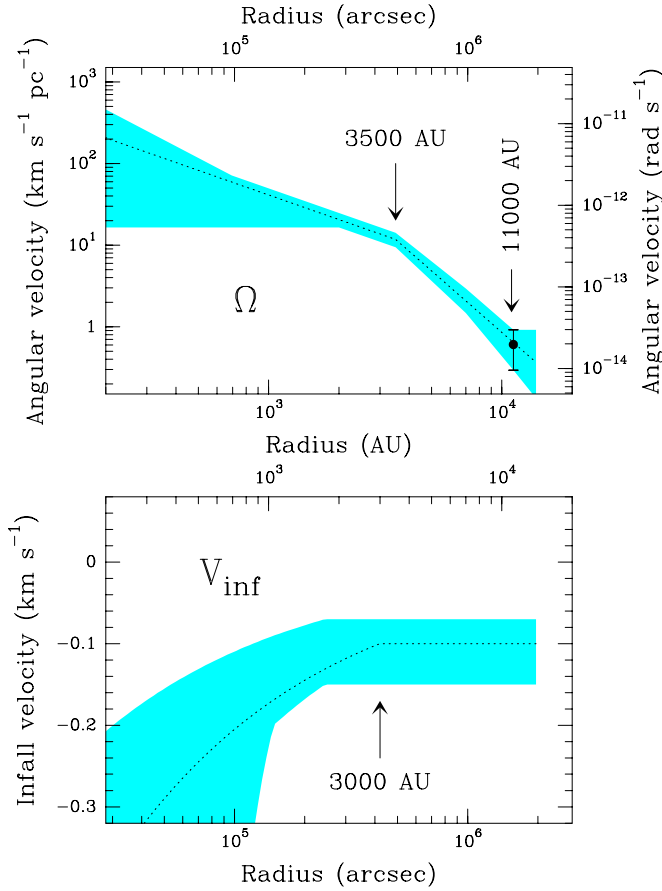


Figure 8. Rotational angular velocity (a) and infall velocity (b) inferred in the IRAM 04191 envelope based on the radiative transfer modeling of Belloche et al. (2002). The shaded areas show the estimated domains where the models match the CS and $C^{34}S$ observations reasonably well.

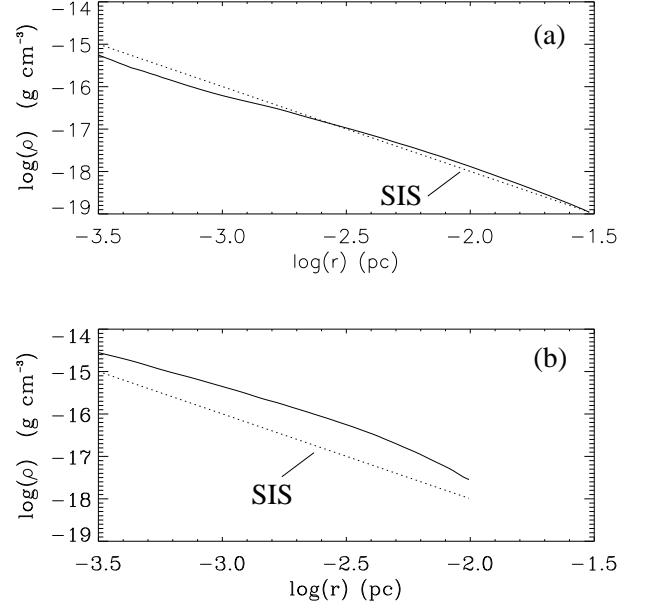


Figure 9. Density profiles (solid curves) obtained slightly after point mass formation ($t \lesssim 10^4$ yr) in SPH numerical simulations of the collapse of a nearly critical $[(\rho_c/\rho_{\text{out}})_{\text{init}} \sim 12]$ isothermal ($T = 10$ K) Bonnor-Ebert sphere induced by external compression (Hennebelle et al. 2002). For comparison, the dotted line shows the $\rho \propto r^{-2}$ profile of a SIS at 10 K. In (a), the collapse was initiated quasi-statically (by very slow compression with $P_{\text{ext}}/\dot{P}_{\text{ext}} = 20 \times$ the initial sound crossing time R_{init}/a_s) and the density profile at $t \gtrsim 0$ is very similar to that of the SIS. By contrast, in (b), the collapse was induced by a very rapid increase in external pressure (with $P_{\text{ext}}/\dot{P}_{\text{ext}} = 0.03 \times R_{\text{init}}/a_s$), resulting in much larger densities around $t \sim 0$.